nature chemistry

ARTICLES

PUBLISHED ONLINE: XX XX 2012 | DOI: 10.1038/NCHEM.1442

Use of the interior cavity of the P22 capsid for site-specific initiation of atom-transfer radical polymerization with high-density cargo loading

Janice Lucon[1,2], Shefah Qazi[1,2], Masaki Uchida[1,2], Gregory J. Bedwell[3], Ben LaFrance[1,2], Peter E. Prevelige Jr[3] and Trevor Douglas[1,2]*

Virus-like particles (VLPs) have emerged as important and versatile architectures for chemical manipulation in the development of functional hybrid nanostructures. Here we demonstrate a successful site-selective initiation of atom-transfer radical polymerization reactions to form an addressable polymer constrained within the interior cavity of a VLP. Potentially, this protein–polymer hybrid of P22 and cross-linked poly(2-aminoethyl methacrylate) could be useful as a new high-density delivery vehicle for the encapsulation and delivery of small-molecule cargos. In particular, the encapsulated polymer can act as a scaffold for the attachment of small functional molecules, such as fluorescein dye or the magnetic resonance imaging (MRI) contrast agent Gd-diethylenetriaminepentacetate, through reactions with its pendant primary amine groups. Using this approach, a significant increase in the labelling density of the VLP, compared to that of previous modifications of VLPs, can be achieved. These results highlight the use of multimeric protein–polymer conjugates for their potential utility in the development of VLP-based MRI contrast agents with the possibility of loading other cargos.

The use of protein–polymer composite materials for medical and materials applications is a growing field that aims to take advantage of the exquisite monodispersity and bioactivity of biomolecules and also impart new material properties via polymer conjugation. When a responsive polymer is selected, new thermo-, light- and pH-sensitive macromolecular materials can be produced to control more fully the activity and phase solubility of the biomolecule[1,2]. By adding a specific polymer to the biomolecule, the composite material may exhibit improved retention, lowered immunogenicity and increased bioavailability[3–5]. To attain the desired final material properties, careful selection of both the protein and the polymer components is essential. Much of this work focused on the site-specific conjugation of polymers to monomeric proteins, but when more complex multimeric biomolecules are employed, not only is the polymer location on the primary sequence of interest, but also the spatial relationship between the polymer and the overall protein architecture becomes increasingly important.

In particular, the use of virus-like particle (VLP) proteins, which are a special class of multimeric proteins that form symmetric protein shells surrounding an empty interior space, relies on two distinct environments that can be modified, either the exposed exterior or the confined interior. For the exterior surface, polymer formation or attachment was employed as a method to append molecules of interest designed to alter VLP solubility, increase stability or introduce new functionalities[6,7]. Electrostatic interactions were used in several systems to package existing polymers or guide capsid assembly around polymers and polymer–nanoparticle composites to provide a charge-dependent occupation of the interior space[8–13]. Previously, synthesis of polymers in the interior space was limited to small protein cages, which were employed as a synthesis chamber for an untethered oligomer or for the development of an anchored addressable network[14,15].

We reported previously the use azide–alkyne 'click' chemistry to construct an anchored polymer network inside a small protein-cage architecture[15–17]. In this stepwise synthesis approach, polymer growth was directed to the protein-cage interior, which resulted in a protein-confined hyperbranched polymer. The protein shell acted as a barrier that limited the polymer size and left only the protein exterior exposed to the bulk solution. By labelling the resulting protein–polymer construct with a Gd-based magnetic resonance imaging (MRI) contrast agent, an enhanced magnetic resonance contrast agent was obtained, which highlights the utility of using the interior space to maximize cargo loading[16]. Although this method is effective, the stepwise nature of the polymerization reaction makes the process onerous for larger constrained polymer syntheses.

A preferable alternative route to achieve an anchored addressable polymer is to proceed via a continuous polymerization of simple monomers from an easily modified initiator. Of the several suitable continuous biomolecule-anchored polymerization methods, we chose to use atom-transfer radical polymerization (ATRP) as it is particularly suited to an improved formation of polymer inside a protein cage. This method is not only rapid, but also results in products with relatively low polydispersity in bulk solutions and is promiscuous with respect to the range of monomers that can be used. Also, the simplicity of the ATRP initiator means that it can be attached readily to the protein cage in a site-specific manner, and thereby we can control the site of polymer initiation. Thus, by combining ATRP with a container-like protein, the formation of a polymer scaffold constrained to the interior of a VLP architecture can be afforded in a single short reaction.

[1]Chemistry and Biochemistry Department, Montana State University, Bozeman, Montana, 59717, USA, [2]Center for Bio-Inspired Nanomaterials, Montana State University, Bozeman, Montana, 59717, USA, [3]Department of Microbiology, University of Alabama at Birmingham, Birmingham, Alabama, 35294, USA. *e-mail: tdouglas@chemistry.montana.edu

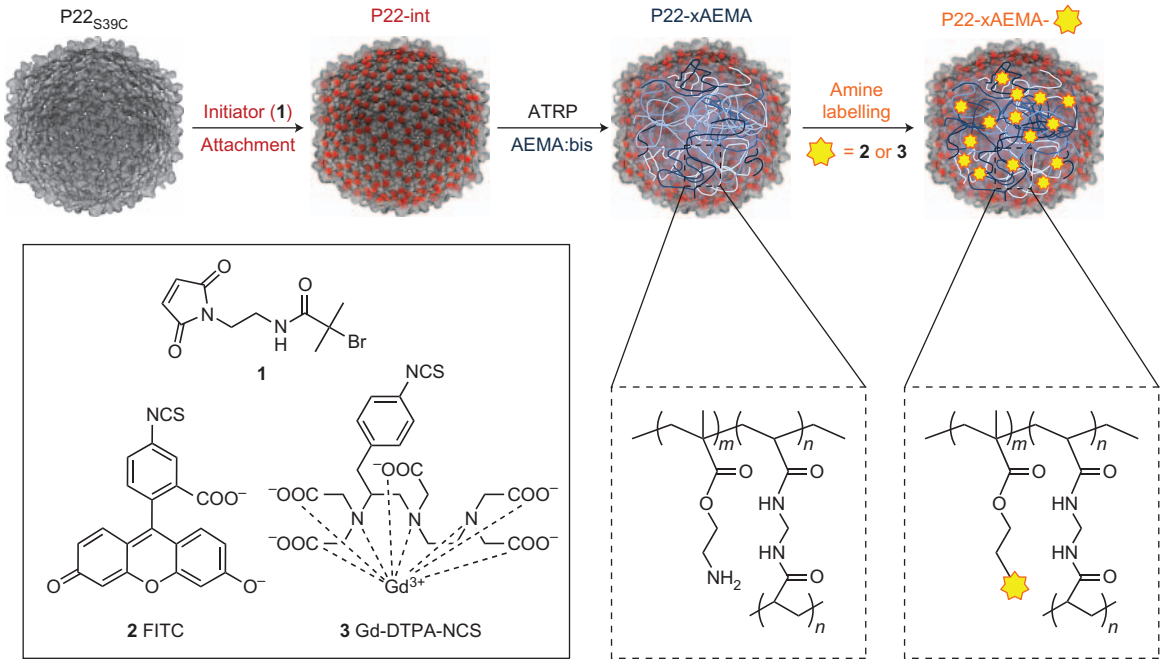

Figure 1 | Schematic of the internally initiated ATRP polymerization within the P22 VLP. $P22_{S39C}$ modified with a cysteine-reactive ATRP initiator (**1**) was used as the macroinitiator and a size-constrained reaction vessel for the ATRP growth of poly(AEMA) strands, cross-linked with bisacrylamide, inside the P22 VLP architecture. Subsequently, this internal polymer scaffold was modified with primary amine-reactive labelling agents, either (**2**) or (**3**), to introduce a high density of new functionality to the construct.

Here we report the use of ATRP to make addressable polymer networks within the confines of the bacteriophage P22-based VLP (Fig. 1). The 2-aminoethyl methacrylate (AEMA) monomer was selected because the primary amine-rich polymer synthesized within the P22 capsid could be modified subsequently with the small molecules of interest, which resulted in very high-density loadings of the capsid. The use of the AEMA network as a scaffold was demonstrated through the attachment of either fluorescein isothiocyanate (FITC) or Gd-DTPA-NCS (DTPA = diethylenetriaminepentacetate). Using this method, we can achieve a substantial increase in the degree of labelling per VLP compared to that given in previous reports, which demonstrates the potential capacity of the capsid interior for directed cargo loading.

Results and discussion

In this work we utilized a VLP (derived from the bacteriophage P22) that consists of 420 subunits arranged on an icosahedral lattice with a resulting exterior diameter of 64 nm and an unoccupied internal cavity with a 54 nm diameter[18]. Recombinant expression in *Escherichia coli* requires co-expression of the coat protein and scaffold protein for self-assembly. This VLP is capable of transformation into a series of distinct morphologies, which includes the procapsid (PC) form that contains the scaffold protein, an empty shell (ES) form in which the scaffold protein is removed, an expanded form (EX) and a wiffle ball (WB) structure in which all 12 pentamers are removed (Supplementary Fig. S1)[19,20]. The EX form most closely mimics the morphology found in the DNA-containing infectious virion and is the form used in this study[20]. To attain the EX form, the scaffold protein is removed from the PC using successive guanidine·HCl extractions followed by heating at 65 °C, which generates the capsid in its EX morphology.

A new P22 mutant was designed for use with ATRP and contained a single-point mutation in the wild-type coat protein $P22_{S39C}$ that introduced an addressable thiol suitable for the attachment of an initiator (**1**). This site was selected specifically such that the introduced thiol could be exposed exclusively to the interior according to the currently available P22 structural models (Fig. 2)[19,21]. Although the wild-type protein contains an intrinsic cysteine (C405) it was not removed because previous studies demonstrated that this site is not addressable[22,23]. This new mutant was characterized and behaves in the same manner as the wild-type P22 capsid, going through the same series of

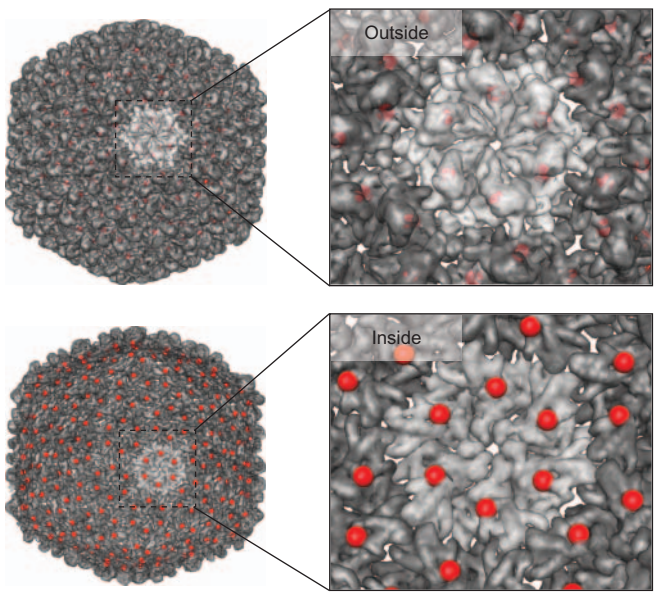

Figure 2 | Structural model of the expanded morphology of the P22 capsid that shows the location of the S39C mutation. The location of the modified residue S39C (in red) was derived from a structural model of P22 using coordinate data[21] deposited as Protein Data Bank file 2XYS. Both a view of the exterior of the capsid (top) and a half shell cut-away view that revealed the interior (bottom) of the capsid are included and illustrate that, according to this model, this mutation site is interior exposed.

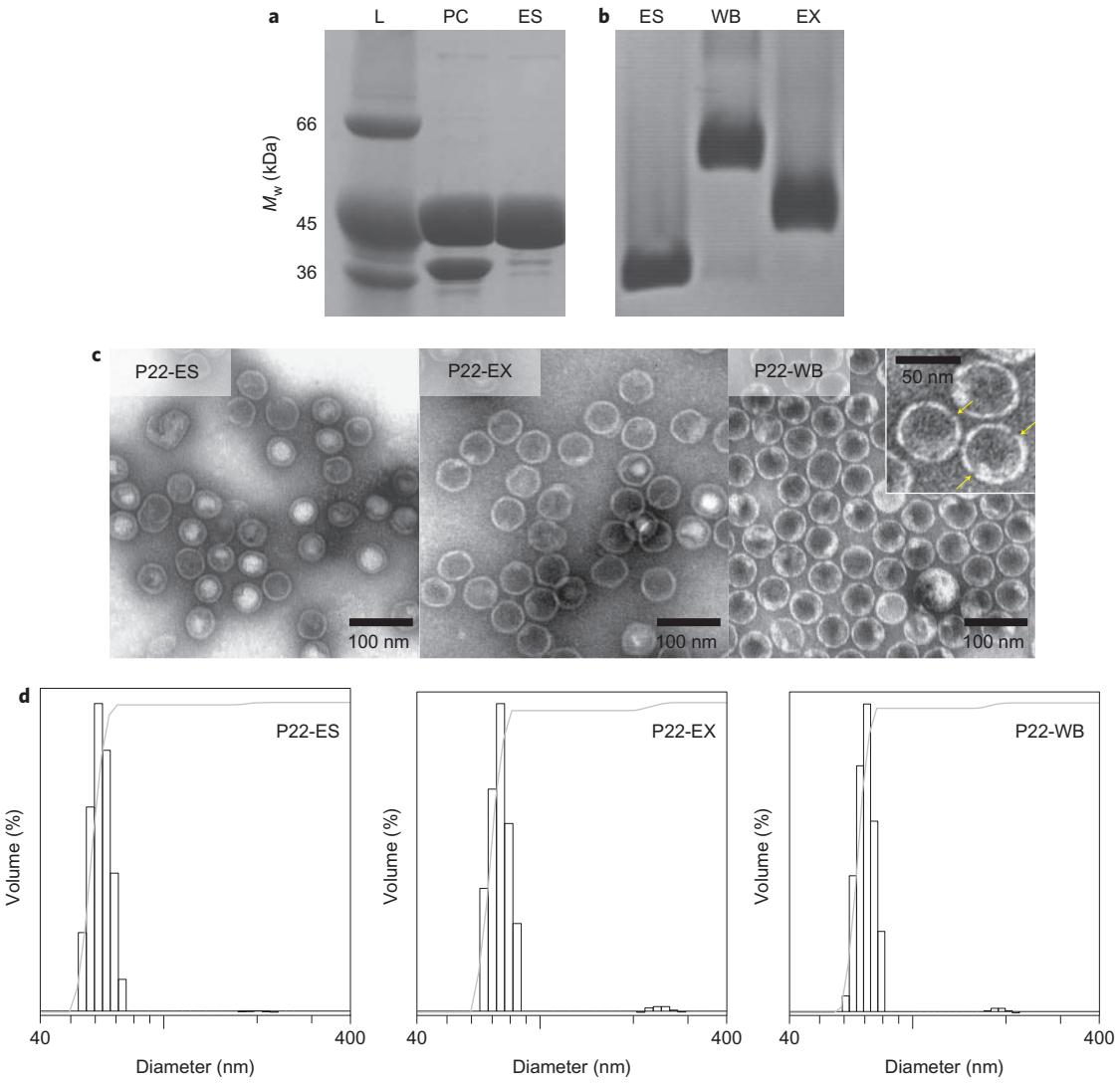

Figure 3 | Characterization of the $P22_{S39C}$ mutant to verify morphological transformation. a, SDS-PAGE of the purified P22 before (PC) and after (ES) extraction of the scaffold protein. The lower band corresponds to the scaffold (33.6 kDa) and the upper band to the coat protein (46.6 kDa). L is the molecular weight standards. **b**, Native agarose gel of the P22 ES, EX and WB structures. The observed shift in mobility indicates the temperature-induced transformation from ES to EX and WB morphologies. **c**, Negatively stained TEM images of the ES, EX and WB morphologies show the degree of particle-size homogeneity. The inset shows the appearance of small voids (yellow arrows) in the shell of the WB morphology. **d**, DLS of the three morphological forms (ES, EX and WB). The measured hydrodynamic diameter for the expansion from ES (60 ± 4 nm) to EX (71 ± 5 nm) and WB (68 ± 4 nm) is as expected.

morphological transformations. To obtain the EX morphology, the scaffold protein was removed from $P22_{S39C}$ to generate the ES, heated to 65 °C and subsequently analysed to ensure the formation of the EX form (Fig. 3). The characteristic shift of the particles to a lower electrophoretic mobility was observed on heating, consistent with expansion of the capsid. Precipitation of the protein was observed only at temperatures greater than 80 °C, which indicates that the protein architecture is relatively thermostable (Supplementary Fig. S2). The size of the VLP, by dynamic light scattering (DLS), increased as expected from 60 ± 4 nm (PC morphology) to 71 ± 5 nm, consistent with the known range of values for the P22 particle in either the EX or WB morphologies (Fig. 3d). By transmission electron microscopy (TEM) the overall structure of the VLP was retained and, after heating to 75 °C, large pores became apparent in the structure (Fig. 3c), which is a characteristic of the WB morphology.

To make the P22 macroinitiator, the $P22_{S39C}$ mutant was labelled with initiator **1**, an amide derivative of a previously reported ATRP initiator. This cysteine-reactive ATRP initiator (Fig. 1) was selected because of its efficient labelling, satisfactory initiation and demonstrated compatibility with biomolecules. Initiator **1**, unlike the ester-containing form previously reported, is expected to be less susceptible to bond cleavage[24,25]. It was synthesized through the modification of established protocols and selectively reacted with $P22_{S39C}$ to make $P22_{S39C}$-int with near-quantitative single labelling of the introduced cysteine, as observed by subunit mass spectrometry (Supplementary Fig. S3).

Using the $P22_{S39C}$-int macroinitiator construct, cross-linked AEMA polymer strands were synthesized inside this protein cage under standard ATRP biomolecule conditions using a Cu(I)/bipyridine catalyst[26]. To explore the range of reaction conditions available to the $P22_{S39C}$ system for internally directed polymerization reactions, initially a selection of AEMA:bisacrylamide monomer to subunit ratios (3,000–26,000) and temperatures (23, 40 and 60 °C), as well as catalyst-loading ratios, were investigated. Samples were monitored by gel electrophoresis and DLS to determine reaction completion and suitable conditions (an example comparison is shown in Supplementary

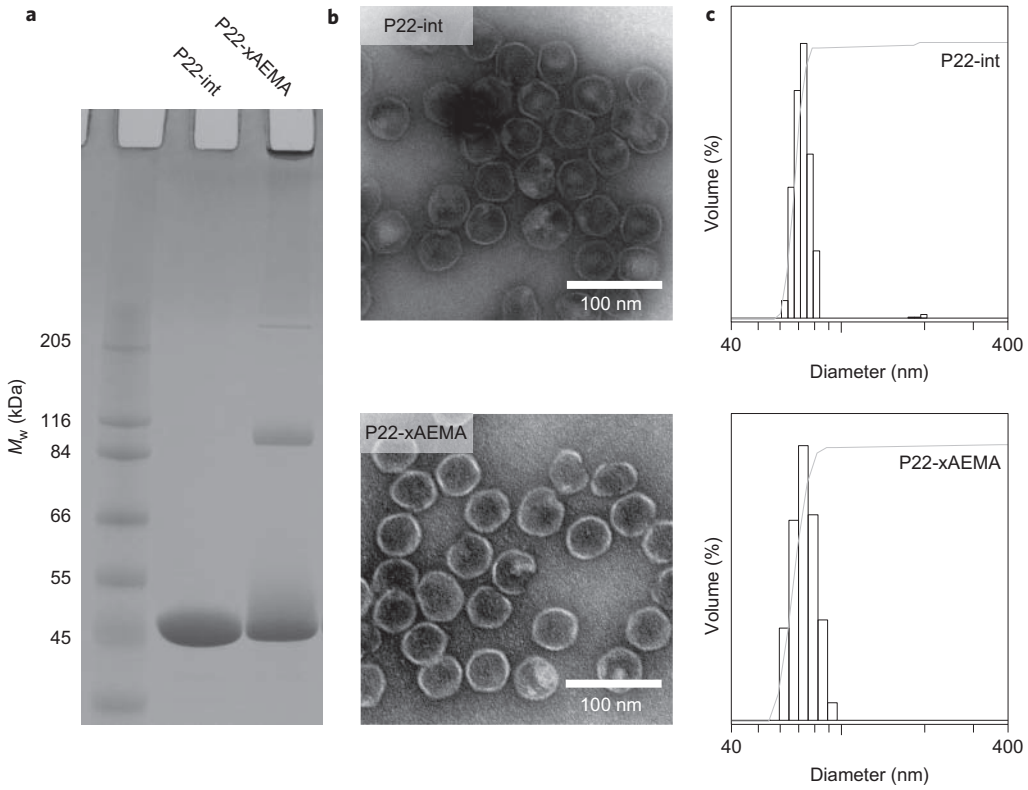

Figure 4 | Size and morphological characterization of the $P22_{S39C}$-xAEMA composite and $P22_{S39C}$-int. a, Representative SDS–PAGE gel of $P22_{S39C}$-int and $P22_{S39C}$-AEMA. The polymerized sample shows some streaking to higher M_w, which indicates the range of polymer chain lengths appended to the subunits as compared to the starting P22. In addition, highly cross-linked material can be observed in the well at the top of the gel. **b**, TEM images of $P22_{S39C}$-int (top) and $P22_{S39C}$-xAEMA (bottom) illustrate that the $P22_{S39C}$-xAEMA retains the size and shape homogeneity of the P22 capsid after the polymerization reaction. **c**, DLS of $P22_{S39C}$-int (top) and $P22_{S39C}$-xAEMA (bottom). The modified sample is monodisperse and has the same average diameter as that of the starting $P22_{S39C}$-int.

Fig. S4). The purified protein–polymer hybrid constructs were stable after polymerization and only at the highest temperature and loading conditions did the diameter of the cage increase significantly, which indicates that under most of the tested conditions the VLP effectively constrains the polymer growth to the interior of the capsid. From these test reactions it was apparent that the monomer loading had a greater impact on the extent of polymerization than the temperature of the reaction, and that the reactions were effectively complete after less than three hours.

To verify further that our selected P22 mutant was confining the polymer, we compared the behaviour of $P22_{S39C}$ to a second mutant of P22 coat protein ($P22_{K118C}$), described previously, and which has a reactive cysteine site predicted to be partially exposed to the exterior (Supplementary Fig. S5)[22]. Both mutants were labelled with an ATRP initiator (Supplementary Figs S6 and S7) and analysed under simple polymerization conditions. We used the uncross-linked AEMA at a loading of 26,000 monomers/subunit of the partially exterior-exposed $P22_{K118C}$, which resulted in dramatically different material properties compared to those of the $P22_{S39C}$ construct under the same conditions and emphasizes the importance of site specificity for polymer initiation and growth in these protein architectures. When the initiator-labelled $P22_{K118C}$ was treated to make $P22_{K118C}$-AEMA, the construct exhibited an increase in diameter of about 20 nm, from 60 ± 3 nm to 81 ± 4 nm, as measured by DLS, which suggests the growth of polymer on the exterior of the cage (Supplementary Fig. S8), but the $P22_{S39C}$-based sample diameter remained constant before (67 ± 4 nm) and after (67 ± 4 nm) polymerization. In addition, unlike $P22_{S39C}$-AEMA, the $P22_{K118C}$-AEMA hybrid was not very stable. Although no precipitation was observed under the reaction conditions, mass precipitation of the $P22_{K118C}$-AEMA occurred on purification. This loss could be alleviated partially by increasing the ionic strength of the buffer (>250 mM NaCl). Taken together, these data support a model in which the initiation site determines the overall access of the AEMA polymer to the exterior environment and when the polymer growth is exposed to the exterior of the cage, the protein–polymer composite destabilizes significantly.

We directed our efforts to the interior-facing $P22_{S39C}$-int macroinitiator construct at a midrange monomer loading (6,000 monomers/subunit) and moderate temperature conditions (23 °C) for further investigation with four experimental replicates. After three hours of reaction time, the synthesis was halted by exposing each sample to air and the protein–polymer conjugate ($P22_{S39C}$-xAEMA) was purified away from the remaining AEMA and bisacrylamide monomers and the copper catalyst by pelleting the protein construct using ultracentrifugation, which easily separates large macromolecular complexes from small molecular species. The resulting construct exhibited a dramatic shift in electrophoretic mobility, by native agarose gel, which indicates that the P22-int had become P22-xAEMA (Fig. S9). On a subunit basis an increased subunit mass (by denaturing gel analysis) was observed, as indicated by a shift to a higher molecular mass (Fig. 4a and Supplementary Fig. S9). By this analysis method, it appears that not all of the initiator-labelled subunits produced sufficiently long polymer chains for a mass shift to be apparent. Others also observed this incomplete initiation in both monomeric and multimeric systems when making grafted-from protein–polymer composites[6,24–26].

To confirm that the polymer was confined to the interior of the P22, the size of the $P22_{S39}$-xAEMA construct was compared to that of the initial macroinitiator P22 complex. When the particles were

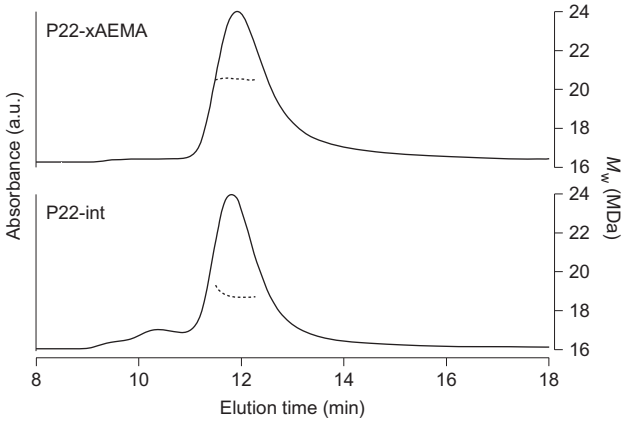

Figure 5 | Molecular weight increase as a result of polymerization, monitored by MALS. Using size-exclusion chromatography, both $P22_{S39C}$-xAEMA and $P22_{S39C}$-int exhibit the same elution time when monitored by absorbance (continuous line) at 280 nm, which indicates retention of the particle size. Fitting the MALS data across the elution profile reveals the molecular weight of the material (dashed line), which increases substantially for the $P22_{S39C}$-xAEMA (top) compared to the $P22_{S39C}$-int (bottom). a.u. = arbitrary units.

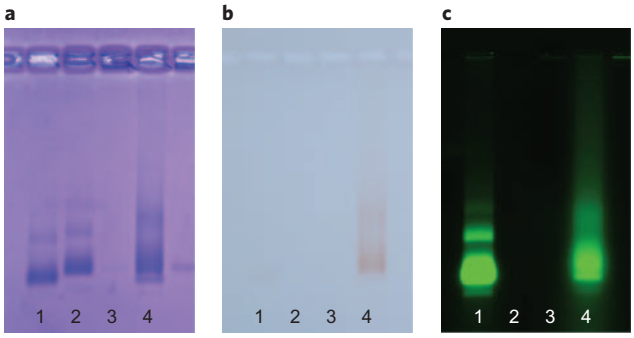

Figure 6 | Polymer formation and covalent modification with FITC was verified by native agarose gel electrophoresis. a–c, Three different views of the same native agarose gel with $P22_{S39C}$-int (lane 1), $P22_{S39C}$-int-FITC (lane 2), $P22_{S39C}$-xAEMA (lane 3) and $P22_{S39C}$-xAEMA-FITC (lane 4). **a**, The gel was stained with Coomassie to detect the protein component. The $P22_{S39C}$-AEMA runs slightly out of the well in the opposite direction to the other proteins because of the net positive charge on the poly(AEMA) at the running buffer pH. Labelling this construct with the negatively charged FITC reverses the effective net charge on the construct and results in a shift in the migration direction. **b**, The unstained gel under ambient light. The $P22_{S39C}$-FITC sample is faintly visible and the $P22_{S39C}$-xAEMA-FITC sample is clearly visible, which signifies the relative degree of FITC labelling in each sample. **c**, The unstained gel illuminated with a laser at 488 nm and detected at 520 nm to highlight FITC. The $P22_{S39C}$-FITC is considerably brighter than the $P22_{S39C}$-xAEMA-FITC, which indicates the relative degree of fluorescence quenching in each sample.

visualized using TEM, the morphology of P22 after the reaction was unchanged from that before (Fig. 4b). The average particle diameter was 51 ± 3 nm in the unpolymerized $P22_{S39C}$-int and remained the same (53 ± 3 nm) after the the reaction. In addition, the hydrodynamic diameter, as measured by DLS, remained unchanged on polymer formation (Fig. 4c). The particle diameters were 70 ± 10 nm and 71 ± 3 nm, respectively, for $P22_{S39C}$-int and $P22_{S39C}$-xAEMA, which further confirms that the polymer was confined to the interior of the protein cage.

Multiangle light scattering (MALS) was used to analyse further the $P22_{S39C}$-xAEMA construct for the radius and molecular weight (Fig. 5). According to this method the radius of the particles remained nearly constant, measured as 29.3 nm ($P22_{S39C}$-int) and 28.2 nm ($P22_{S39C}$-xAEMA), but the molecular weight increased on polymerization. Using the standard refractive index increment (dn/dc) for protein (0.185) and the published value for AEMA (0.153) (ref. 27), the MALS data from the $P22_{S39C}$-int and $P22_{S39C}$-xAEMA samples were fitted to obtain molecular weights. The measured molecular weight for $P22_{S39C}$-int was 18.9 ± 0.2 MDa, consistent with the predicted value for the EX morphology of P22, but the $P22_{S39C}$-xAEMA had a combined molecular weight of 20.2 ± 0.6 MDa, with 18.7 ± 0.5 MDa contributed from the protein and 1.5 ± 0.4 MDa contributed from the polymer. This mass increase corresponds to the addition of $12{,}000 \pm 3{,}000$ AEMA monomers/VLP or 28 ± 7 AEMA monomers/subunit, on average.

The internally directed $P22_{S39C}$-xAEMA polymerization resulted in the introduction of a large number of addressable amines sequestered within the protein cage. To demonstrate that the introduced amines on the poly-AEMA inside the $P22_{S39C}$-xAEMA construct were addressable, FITC (**2**) was used as an amine-specific labelling agent. Both the $P22_{S39C}$-xAEMA and $P22_{S39C}$-int control were incubated with a 100-fold excess of FITC per subunit to give $P22_{S39C}$-xAEMA-FITC and $P22_{S39C}$-FITC, respectively. Excess FITC was removed by pelleting the protein twice using ultracentrifugation followed by resuspension before analysis. The difference in the degree of labelling between the $P22_{S39C}$-FITC and $P22_{S39C}$-xAEMA-FITC was significant enough to be readily discernible (Supplementary Fig. S10).

When the fluorescently labelled $P22_{S39C}$-xAEMA construct was analysed using gel electrophoresis the fluorescein signal was observed to migrate with the protein. Under denaturing sodium dodecyl sulfate polyacrylamide gel electrophoresis (SDS–PAGE) conditions, the fluorescein migrated with the subunit and with the polymer-modified subunit, which indicates that the fluorescent dye was bound covalently to the construct and not just sorbed onto the protein–polymer composite (Supplementary Fig. S11). When analysed by native agarose gel electrophoresis, a net shift in the electrophoretic mobility of the $P22_{S39C}$-xAEMA and $P22_{S39C}$-xAEMA-FITC was observed, caused by the polymer and FITC altering the charge of the construct (Fig. 6a). The observed shift indicates that the polymer and dye were associated tightly with the protein cage. The $P22_{S39C}$-xAEMA-FITC was labelled to the extent that the migration of a distribution of species was visible prior to staining under ambient light, but $P22_{S39C}$-FITC was observed only weakly (Fig. 6b). In contrast, the emission signal of the $P22_{S39C}$-xAEMA-FITC distribution was depressed in intensity compared to that of the much less heavily labelled $P22_{S39C}$-FITC (Fig. 6c), which probably results from self-quenching of the fluorophore caused by the abundance of polymer-bound fluorescein in close proximity. This apparent loss of fluorescence intensity was confirmed by solution-phase analysis of the constructs, in which a greater than 95% reduction in fluorescence was observed in the $P22_{S39C}$-xAEMA-FITC compared to $P22_{S39C}$-FITC (Supplementary Fig. S12). Similar quenching was shown in systems with high fluorophore concentrations, such as micelles, where derivatives of fluorescein can lose more than 98% of their fluorescence signal because of proximity and dimerization effects[28,29].

After demonstrating polymerization within the P22 capsid and the postsynthetic modification of the functional groups, we explored the $P22_{S39C}$-xAEMA composite system as a potential T_1 contrast agent through the attachment of Gd-DTPA-NCS (**3**) to the encapsulated polymer. Gd-DTPA-NCS was added, in a 100-fold excess per subunit, to the $P22_{S39C}$-AEMA or $P22_{S39C}$-int and allowed to react overnight, followed by pelleting by ultracentrifugation and resuspension of the protein twice in each of four experimental replicates. The resulting material ($P22_{S39C}$-xAEMA-Gd or $P22_{S39C}$-int-Gd)

was analysed for both sulfur and gadolinium content by inductively couple plasma mass spectrometry (ICP-MS) to determine both the Gd and protein concentrations. To rule out the possibility of simple electrostatic interaction between the polymer and Gd-DTPA, controls with both $P22_{S39C}$-xAEMA and $P22_{S39C}$-int were incubated and isolated, under the same conditions as above, with Magnevist (Gd-DTPA), which lacks the amine-reactive isothiocyanate. When these constructs were analysed by native agarose gel electrophoresis (Supplementary Fig. S13), a net shift in the electrophoretic mobility of the $P22_{S39C}$-xAEMA-Gd was observed, caused by the polymer and Gd-DTPA-NCS altering the net charge of the construct, but the $P22_{S39C}$-xAEMA-Magnevist sample retained the same low electrophoretic mobility as that of the $P22_{S39C}$-xAEMA, which provides evidence that there were no significant electrostatic interactions between $P22_{S39C}$-xAEMA and Gd-DTPA.

The Gd-DTPA loading per P22 was determined quantitatively for each of the constructs from the ICP-MS data. The $P22_{S39C}$-xAEMA-Gd contained 28 times more Gd/VLP than the $P22_{S39C}$-int-Gd control (320 Gd/VLP, <1 Gd/subunit), where endogenous lysines were modified, which indicated that it is largely the polymer that is being labelled rather than the protein shell. The low reactivity of the endogenous P22 lysines was reported previously, with only a few of the 20 lysines per subunit observed to be reactive[30]. This minimal background reactivity is advantageous because it means that in the $P22_{S39C}$-AEMA sample the vast majority (>95%) of the addressable sites are located on the encapsulated polymer. If necessary, endogenous lysines could be blocked chemically prior to polymerization[15]. The $P22_{S39C}$-xAEMA-Gd loading per cage was $9{,}100 \pm 800$ Gd/VLP (22 ± 2 Gd/subunit), which corresponds to an internal concentration of 150 mM Gd within the VLP. This is significantly more Gd, both on a per-cage and per-subunit basis, than that in previous reports using VLPs, with values that ranged from less than 1.0/subunit to 6.6/subunit (60/VLP to 650/VLP), and highlights the advantage of using the full capacity of the interior volume[6,16,31–37]. In addition, both the $P22_{S39C}$-xAEMA and $P22_{S39C}$-int incubated with Magnevist (Gd-DTPA) contained Gd levels below the lower limit of quantification, which demonstrates that the Gd detected is attached covalently to the protein–polymer construct rather than associated via electrostatic interactions under the labelling reaction conditions.

To verify that the high loading observed was reasonable and occurred homogeneously across the population of P22 capsids, the particles were analysed by analytical ultracentrifugation to investigate differences in sedimentation velocity (Fig. 7). The measured sedimentation value of the $P22_{S39C}$-xAEMA (167 S) falls within the range observed for $P22_{S39C}$-int (142 S) and the scaffold protein that contains PC morphology (191 S), which indicates that the polymer content does not exceed the packing observed in the naturally occurring self-assembled system. Covalent modification of polymer with Gd-DTPA-NCS to make $P22_{S39C}$-xAEMA-Gd resulted in a shift to a higher S value (227 S), which is consistent with the efficient incorporation of additional mass via Gd-DTPA-NCS to the interior of the VLP.

The ^{1}H relaxivity of water in the presence of these highly loaded $P22_{S39C}$-xAEMA-Gd particles and $P22_{S39C}$-int-Gd control was measured at 60 MHz (1.4 T), using an inversion recovery-pulse sequence. The $P22_{S39C}$-xAEMA-Gd and $P22_{S39C}$-int-Gd had ionic relaxivities (r_1) of 22.0 $mM^{-1}\,s^{-1}$ and 23.5 $mM^{-1}\,s^{-1}$, respectively. The observed improvement in r_1 for both constructs is consistent with an enhancement over free Gd-DTPA (4.0 $mM^{-1}\,s^{-1}$), which corresponds to an increase in the rotational correlation time that arises from tethering the chelate to a large supramolecular particle[16,35]. In addition, because the ionic relaxivity is enhanced similarly in both constructs it can be concluded that the polymer does not restrict water exchange significantly between the bulk and the interior of the $P22_{S39C}$-xAEMA-Gd composite, as water restriction would lessen the observed enhancement, as is seen in some micelles and liposomes[38,39].

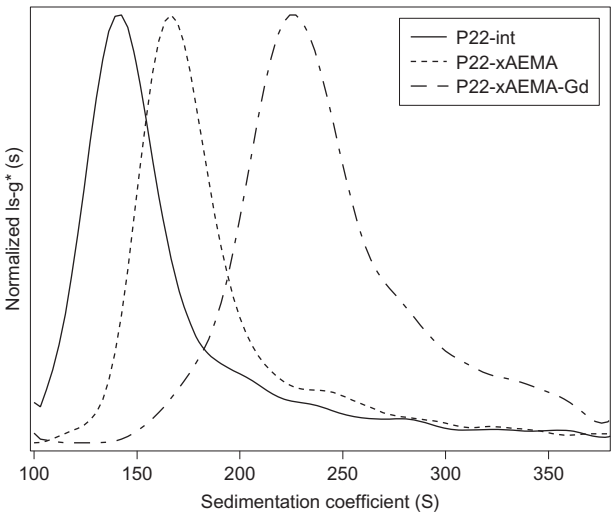

Figure 7 | Analysis of sample population homogeneity by analytical ultracentrifugation. Samples were centrifuged at 5,000–7,000 r.p.m. and absorbance data were acquired at 280 nm to attain sedimentation values for each sample. The measured sedimentation value of the $P22_{S39C}$-xAEMA (167 S) shows an increase from that of $P22_{S39C}$-int (142 S) and covalent modification of polymer with Gd-DTPA-NCS to make $P22_{S39C}$-xAEMA-Gd resulted in a shift to a higher S value (227 S), consistent with the incorporation of additional mass via Gd-DTPA-NCS labelling of the polymer. These data indicate that there is a homogeneous shift in the entire population to higher S values with each modification.

In addition to the ionic relaxivity enhancement, each $P22_{S39C}$-xAEMA-Gd carries $9{,}100 \pm 800$ Gd/VLP, which leads to a per particle relaxivity of 200,000 $mM^{-1}\,s^{-1}$. The particle relaxivity of $P22_{S39C}$-xAEMA-Gd dramatically exceeds that of the $P22_{S39C}$-int-Gd control (7,500 $mM^{-1}\,s^{-1}$) and those in previous reports of VLP nanoparticle-based MRI contrast agents, with values that fall in the range of 10^3–10^4 $mM^{-1}\,s^{-1}$ (refs 6,16,31–37). The particle relaxivity is also higher than those observed for many other macromolecular assemblies, such as micelles, liposomes and polymers, which places this construct comfortably in the upper end of observed macromolecular relaxivities for its size[38–42].

Conclusions

In summary, the application of ATRP for site-directed polymer formation inside a VLP results in an anchored network that is unparalleled for labelling purposes and utilizes the previously largely untapped interior volume of the VLP. The $P22_{S39C}$-based macroinitiator effectively directs polymer growth to the VLP interior, which results in a confined polymer growth because the protein shell acts as a barrier to unconstrained polymer growth, to leave only the protein shell exposed to the bulk solution. By selecting an appropriate macroinitiator and monomer, this new multimeric protein–polymer composite acts as a scaffold for the attachment of small molecules of interest, such as the fluorophore FITC or paramagnetic MRI contrast agents (here, Gd-DTPA-NCS). The introduced polymer scaffold results in a significantly increased number of labels per cage compared to those of other VLP-based systems. The improvement in labelling is important for the delivery of contrast agent on a per-particle basis as it allows for a high concentration delivery of contrast agent or other cargo molecules of interest. This material exhibits an order-of-magnitude improvement in relaxivity per particle over that of existing VLP systems. The use of this material as a targeted MRI contrast agent is particularly

interesting because of the high relaxivity and is an application we are exploring further. As a consequence of the simplicity, modular nature and loading level of the ATRP-based approach taken to make these P22–polymer internal composites, currently this same method is being employed to make a range of novel VLP–polymer composites with biomedical and catalytic applications.

Methods. All materials were analytical grade and purchased from either Sigma-Aldrich or Fisher Scientific and used as received unless otherwise noted. Dichloromethane was distilled over calcium hydride prior to use. All water was deionized using a NANOpure water-purification system. DLS measurements were taken on a 90Plus particle-size analyser (Brookhaven) and the data were processed by volume distribution.

Synthesis of 2-bromoisobutyryl aminoethyl maleimide (1). 1 was synthesized by a modification of the procedures reported previously[24,25]. *N*-2-aminoethylmaleimide (250 mg, 0.98 mmol) was mixed on ice with triethylamine (300 μl, 2.2 mmol) in 5 ml dry dichloromethane. 2-bromo-2-methylpropionylbromide (200 μl, 1.6 mmol) was added dropwise. The reaction was allowed to warm to room temperature and subsequently extracted three times from dichloromethane and water, followed by drying over anhydrous sodium sulfate. The crude product was cleaned via column chromatography (silica gel, 10% ethyl acetate in dichloromethane) with a yield of 80%. ^{1}H NMR (500 MHz, $CDCl_3$) $\delta = 1.89$ (s, 6H, CH_3); 3.46 (dd, $J = 5.5, 5.5$, 2H, NCH_2); 3.72 (dd, $J = 5.0, 1.5$, 2H, NCH_2); 6.71 (s, 2H, CH_{vinyl}), 6.97 (s, NH). ^{13}C $\delta = 32.54$ (CH_3), 37.34 (NCH_2), 39.84 (NCH_2), 62.51 (C), 134.59(CH_{vinyl}), 170.96 (CO), 172.74 (CO). Electrospray ionization mass spectrometry: m/z calculated 289.0188, 291.0167 (MH^+), found m/z 289.0192, 291.0179.

P22-int macroinitiator formation conditions. $P22_{S39C}$ in PBS, pH 7.6 (4 ml, 7.2 mg ml^{-1}) was infused with 156 μl of **1** (80 mM in DMSO, tenfold excess per subunit). The mixture was allowed to react for three hours at room temperature. After three hours the reaction was quenched with dithiothreitol (DTT) (156 μl, 80 mM in water). To remove excess DTT and **1**, the protein was pelleted at 48,000 revolutions per minute (r.p.m.) for 50 minutes in an ultracentrifuge (Sorvall) followed by resuspension into PBS, pH 7.6. By subunit mass spectrometry, >95% of the subunits were labelled. The yield was quantitative.

P22-AEMA polymer formation conditions. Each experimental replicate was made in a large crimp-top vial with the addition of 20 ml monomer solution (4 wt% 16:4 AEMA:bisacrylamide in PBS, pH 8.0) and 11 ml buffer (PBS, pH 8.0), followed by pH adjustment with concentrated sodium hydroxide solution, as needed, back to pH 8.0. To this mixture, 6 ml of P22-int (8.0 mg ml^{-1}, 1.0 μmol subunit, pH 8.0) was added followed by pumping and back-filling with Ar four times to de-aerate the mixture. The metal catalyst solution was made in a second crimp vial with 19.2 mg CuBr (0.13 mmol), 29.9 mg $CuBr_2$ (0.13 mmol) and 83.5 mg 2,2′-bipyridine (0.53 mmol) followed by the addition of 10 ml deionized water, which had been degassed by bubbling Ar through the liquid for 20 minutes. Subsequently, the vial was sonicated for five minutes to obtain a dark-brown solution. To the monomer–protein vial, 3 ml of the metal catalyst solution was added and the vial maintained at 23 °C for the remaining duration of the experiment. After three hours the reaction was quenched by exposure to air and the protein–polymer composite was purified away from the unreacted monomer and copper catalyst by pelleting and resuspending the protein twice in 100 mM sodium carbonate with 50 mM NaCl buffer, pH 9.0. The yield was 38.7 mg (81%).

FITC (2) labelling conditions. To 2.0 ml $P22_{S39C}$-xAEMA (0.086 μmol subunit, carbonate buffer, pH 9.0) at 2 mg ml^{-1}, 343 μl FITC (8.6 mmol, 25 mM in DMSO) was added dropwise to the vortexing protein solution. The mixture was allowed to sit overnight at 4 °C followed by purification away from excess FITC by pelleting and resuspending (carbonate buffer, pH 9.0) the protein twice over.

Gd-DTPA-NCS (3) labelling conditions. Gd-DTPA-NCS was made according to established procedures[16]. Briefly, 2.80 mg (4.31 μmol) DTPA-NCS was dissolved in 40 μl 1M sodium bicarbonate and 200 μl water. Once the DTPA-NCS dissolved completely, 5.27 μl $GdCl_3$ (900 mM in water, 4.74 μmol) was added to the solution and stirred for three hours at room temperature. The solution was subsequently diluted to 10 mM with DMSO (186 μl) and added to the protein–polymer conjugate as follows. To 4.0 ml of $P22_{S39C}$-AEMA (0.17 μmol subunit, 2 mg ml^{-1} carbonate buffer, pH 9.0), 1,700 μl (17 μmol) Gd-DTPA (10 mM in DMSO/H_2O) was added dropwise to the vortexing protein solution. The mixture was allowed to sit overnight at 4 °C followed by purification away from excess Gd-DTPA by pelleting and resuspending the protein twice. The yield was 5.2 mg (65%).

MALS. P22-int and P22-xAEMA samples were separated over a WTC-0100S (Wyatt Technologies) size-exclusion column at a flow rate of 0.7 ml min^{-1} (Agilent 1200 HPLC) in 50 mM phosphate, 500 mM sodium chloride, pH 8.0. Each sample injection was 25 μl and the samples were run in triplicate. Elution profiles for mass analysis were detected using an ultraviolet–visible detector (Agilent), a Wyatt HELEOS MALS detector and a Wyatt Optilab rEX differential refractometer. Using the elution-profile data the number-averaged molecular mass was calculated with Astra 5.3.14 software (Wyatt Technologies) using a dn/dc for protein of 0.185 and a dn/dc for the polymer component of 0.153 (ref. 27)

Protein and Gd concentrations. The protein concentration was determined by analysing samples for sulfur content and the Gd concentration by ICP-MS at Energy Labs (Billings, MT). Samples were submitted in triplicate and average concentrations reported. The protein concentration was obtained by subtracting the Gd contribution that resulted from sulfur in the DTPA-NCS chelator from the total detected sulfur concentration. The remaining sulfur content was converted into subunit concentration using a conversion factor of 13 thiols per subunit (according to mass spectrometry, the initial Met in the P22 coat sequence is not present in the final protein).

Received 12 August 2011; accepted 23 July 2012; published online XX XX 2012

References

1. Grover, G. N. & Maynard, H. D. Protein–polymer conjugates: synthetic approaches by controlled radical polymerizations and interesting applications. *Curr. Opin. Chem. Biol.* **14,** 818–827 (2010).
2. Krishna, O. D. & Kiick, K. L. Protein- and peptide-modified synthetic polymeric biomaterials. *Biopolymers* **94,** 32–48 (2010).
3. Thordarson, P., Le Droumaguet, B. & Velonia, K. Well-defined protein–polymer conjugates – synthesis and potential applications. *Appl. Microbiol. Biotechnol.* **73,** 243–254 (2006).
4. Depp, V., Alikhani, A., Grammer, V. & Lele, B. S. Native protein-initiated ATRP: a viable and potentially superior alternative to PEGylation for stabilizing biologics. *Acta Biomater.* **5,** 560–569 (2009).
5. Klok, H. A. Peptide/protein-synthetic polymer conjugates: *quo vadis*. *Macromolecules* **42,** 7990–8000 (2009).
6. Pokorski, J. K., Breitenkamp, K., Liepold, L. O., Qazi, S. & Finn, M. G. Functional virus-based polymer–protein nanoparticles by atom transfer radical polymerization. *J. Am. Chem. Soc.* **133,** 9242–9245 (2011).
7. Schlick, T. L., Ding, Z. B., Kovacs, E. W. & Francis, M. B. Dual-surface modification of the tobacco mosaic virus. *J. Am. Chem. Soc.* **127,** 3718–3723 (2005).
8. de la Escosura, A., Nolte, R. J. M. & Cornelissen, J. Viruses and protein cages as nanocontainers and nanoreactors. *J. Mater. Chem.* **19,** 2274–2278 (2009).
9. Aniagyei, S. E., DuFort, C., Kao, C. C. & Dragnea, B. Self-assembly approaches to nanomaterial encapsulation in viral protein cages. *J. Mater. Chem.* **18,** 3763–3774 (2008).
10. Dixit, S. K. *et al.* Quantum dot encapsulation in viral capsids. *Nano Lett.* **6,** 1993–1999 (2006).
11. Comellas-Aragones, M. *et al.* Controlled integration of polymers into viral capsids. *Biomacromolecules* **10,** 3141–3147 (2009).
12. Douglas, T. & Young, M. Host–guest encapsulation of materials by assembled virus protein cages. *Nature* **393,** 152–155 (1998).
13. Hu, Y. F., Zandi, R., Anavitarte, A., Knobler, C. M. & Gelbart, W. M. Packaging of a polymer by a viral capsid: the interplay between polymer length and capsid size. *Biophys. J.* **94,** 1428–1436 (2008).
14. Abe, S. *et al.* Polymerization of phenylacetylene by rhodium complexes within a discrete space of apo-ferritin. *J. Am. Chem. Soc.* **131,** 6958–6960 (2009).
15. Abedin, M. J., Liepold, L., Suci, P., Young, M. & Douglas, T. Synthesis of a cross-linked branched polymer network in the interior of a protein cage. *J. Am. Chem. Soc.* **131,** 4346–4354 (2009).
16. Liepold, L. O. *et al.* Supramolecular protein cage composite MR contrast agents with extremely efficient relaxivity properties. *Nano Lett.* **9,** 4520–4526 (2009).
17. Lucon, J. *et al.* A click chemistry based coordination polymer inside small heat shock protein. *Chem. Commun.* **46,** 264–266 (2010).
18. Earnshaw, W., Casjens, S. & Harrison, S. C. Assembly of head of bacteriophage P22: X-ray diffraction from heads, proheads and related structures. *J. Mol. Biol.* **104,** 387–410 (1976).
19. Parent, K. N. *et al.* P22 coat protein structures reveal a novel mechanism for capsid maturation: stability without auxiliary proteins or chemical crosslinks. *Structure* **18,** 390–401 (2010).
20. Teschke, C. M., McGough, A. & Thuman-Commike, P. A. Penton release from P22 heat-expanded capsids suggests importance of stabilizing penton–hexon interactions during capsid maturation. *Biophys J* **84,** 2585–2592 (2003).
21. Chen, D. H. *et al.* Structural basis for scaffolding-mediated assembly and maturation of a dsDNA virus. *Proc. Natl Acad. Sci. USA* **108,** 1355–1360 (2011).
22. Kang, S. *et al.* Implementation of P22 viral capsids as nanoplatforms. *Biomacromolecules* **11,** 2804–2809 (2010).
23. Tuma, R., Prevelige, P. E. & Thomas, G. J. Mechanism of capsid maturation in a double-stranded DNA virus. *Proc. Natl Acad. Sci. USA* **95,** 9885–9890 (1998).
24. Mantovani, G. *et al.* Design and synthesis of *N*-maleimido-functionalized hydrophilic polymers via copper-mediated living radical polymerization: a suitable alternative to PEGylation chemistry. *J. Am. Chem. Soc.* **127,** 2966–2973 (2005).

25. Heredia, K. L. *et al. In situ* preparation of protein: 'Smart' polymer conjugates with retention of bioactivity. *J. Am. Chem. Soc.* **127,** 16955–16960 (2005).
26. Peeler, J. C. *et al.* Genetically encoded initiator for polymer growth from proteins. *J. Am. Chem. Soc.* **132,** 13575–13577 (2010).
27. Alidedeoglu, A. H., York, A. W., Rosado, D. A., McCormick, C. L. & Morgan, S. E. eBioconjugation of D-glucuronic acid sodium salt to well-defined primary amine-containing homopolymers and block copolymers. *J. Polym. Sci. A* **48,** 3052–3061 (2010).
28. Weinstein, J. N., Yoshikami, S., Henkart, P., Blumenthal, R. & Hagins, W. A. Liposome–cell interaction: transfer and intracellular release of a trapped fluorescent marker. *Science* **195,** 489–492 (1977).
29. Chen, R. F. & Knutson, J. R. Mechanism of fluorescence concentration quenching of carboxyfluorescein in liposomes: energy transfer to nonfluorescent dimers. *Anal. Biochem.* **172,** 61–77 (1988).
30. Kang, S., Hawkridge, A. M., Johnson, K. L., Muddiman, D. C. & Prevelige, P. E. Identification of subunit–subunit interactions in bacteriophage P22 procapsids by chemical cross-linking and mass spectrometry. *J. Proteome Res.* **5,** 370–377 (2006).
31. Allen, M. *et al.* Paramagnetic viral nanoparticles as potential high-relaxivity magnetic resonance contrast agents. *Magn. Reson. Med.* **54,** 807–812 (2005).
32. Liepold, L. *et al.* Viral capsids as MRI contrast agents. *Magn. Reson. Med.* **58,** 871–879 (2007).
33. Anderson, E. A. *et al.* Viral nanoparticles donning a paramagnetic coat: conjugation of MRI contrast agents to the MS2 capsid. *Nano Lett.* **6,** 1160–1164 (2006).
34. Prasuhn, D. E., Yeh, R. M., Obenaus, A., Manchester, M. & Finn, M. G. Viral MRI contrast agents: coordination of Gd by native virions and attachment of Gd complexes by azide–alkyne cycloaddition. *Chem. Commun.* 1269–1271 (2007).
35. Datta, A. *et al.* High relaxivity gadolinium hydroxypyridonate–viral capsid conjugates: nanosized MRI contrast agents. *J. Am. Chem. Soc.* **130,** 2546–2552 (2008).
36. Hooker, J. M., Datta, A., Botta, M., Raymond, K. N. & Francis, M. B. Magnetic resonance contrast agents from viral capsid shells: a comparison of exterior and interior cargo strategies. *Nano Lett.* **7,** 2207–2210 (2007).
37. Dunand, F. A., Borel, A. & Helm, L. Gd(III) based MRI contrast agents: improved physical meaning in a combined analysis of EPR and NMR data? *Inorg. Chem. Commun.* **5,** 811–815 (2002).
38. Mulder, W. J. M., Strijkers, G. J., van Tilborg, G. A. F., Griffioen, A. W. & Nicolay, K. Lipid-based nanoparticles for contrast-enhanced MRI and molecular imaging. *NMR Biomed.* **19,** 142–164 (2006).
39. Ghaghada, K. B. *et al.* New dual mode gadolinium nanoparticle contrast agent for magnetic resonance imaging. *PLoS One* **4,** 1–7 (2009).
40. Karfeld-Sulzer, L. S., Waters, E. A., Davis, N. E., Meade, T. J. & Barron, A. E. Multivalent protein polymer MRI contrast agents: controlling relaxivity via modulation of amino acid sequence. *Biomacromolecules* **11,** 1429–1436 (2010).
41. Schuhmanngiampieri, G., Schmittwillich, H., Frenzel, T., Press, W. R. & Weinmann, H. J. *In vivo* and *in vitro* evaluation of Gd-DTPA-polylysine as a macromolecular contrast agent for magnetic resonance imaging. *Invest. Radiol.* **26,** 969–974 (1991).
42. Ananta, J. S. *et al.* Geometrical confinement of gadolinium-based contrast agents in nanoporous particles enhances T(1) contrast. *Nature Nanotech.* **5,** 815–821 (2010).

Acknowledgements

This research was supported in part by grants from the National Institutes of Health (R01-EB012027), the National Science Foundation (CBET-0709358) and a National Science Foundation Graduate Research Fellowship (J.L.). P.E.P. and G.J.B. were supported by the US Department of Energy, Office of Basic Energy Sciences, Division of Materials Sciences and Engineering (DE-FG02-08ER46537).

Author contributions

J.L. designed and carried out the experiments. S.Q. characterized the samples by NMR and analysed the relaxivity data. M.U. and B.L.F. assisted in the initial characterization of the S39C mutant. G.J.B. characterized the samples by analytical ultracentrifugation. M.U. and T.D. assisted in the experimental design. J.L. and T.D. co-wrote the manuscript. P.E.P. and T.D. coordinated the project. All authors discussed the results.

Additional information

Supplementary information and chemical compound information are available in the online version of the paper. Reprints and permission information is available online at http://www.nature.com/reprints. Correspondence and requests for materials should be addressed to T.D.

Competing financial interests

The authors declare no competing financial interests. Q3

PUBLISHER: **Nature**

PAPER NO. NCHEM-1442

AUTHORS: Trevor Douglas

PAPER TITLE: Use of the interior cavity of the P22 capsid for site-specific initiation of atom transfer radical polymerization with high-density cargo loading

Author queries

AUTHOR MANUSCRIPT PAGE	NO.	QUERIES	REPLY
Title	1	The Editor has changed the title to avoid ambiguity.	
Results and discussion, sixth paragraph, second sentence	2	Please define 'xAEMA' at its first mention in the text and check the use of 'xAEMA' and 'AEMA' is consistent throughout.	
Competing financial interests	3	Please confirm this statement is correct.	
Fig. 5 caption	4	I have inserted '(a.u.)' after Absorbance and defined this as arbitrary units in the caption, OK? If not, please amend as necessary.	